Multiplexed photon-counting computed tomography enabled by spectrally orthogonal contrast nanomaterials

Min Jun Ko[1,‡+], Kihong Son[2,‡], Jun-Hyeok Han[1], Sanghee Lee[1++], Minji Ahn[1], Woojin Back[3], Amir A. Borhani[1], Andrew C. Gordon[1], Robert J. Lewandowski[1], Ji-Ho Park[3], Dong-Hyun Kim[1,4,5,6,]*

[1]Department of Radiology, Feinberg School of Medicine, Northwestern University, Chicago, 60611 USA.

[2]Medical Information Research Section, Electronics and Telecommunications Research Institute (ETRI), Daejeon 34129, Republic of Korea.

[3]Department of Bio and Brain Engineering, Korea Advanced Institute of Science and Technology (KAIST), Daejeon 34141, Republic of Korea.

[4]Robert H. Lurie Comprehensive Cancer Center, Northwestern University, Chicago, IL 60611, USA.

[5]Department of Biomedical Engineering, McCormick School of Engineering, Northwestern University, Evanston, IL 60208, USA.

[6]Department of Biomedical Engineering, University of Illinois, Chicago, IL 60607, USA

[*]E-mail: dhkim@northwestern.edu

[+]Current address: School of Materials Science and Engineering, Kumoh National Institute of Technology, Gumi-si, Gyeongsangbuk-do 39177, Republic of Korea

[++]Current address: School of Nanomedical Engineering, Korea National University of Transportation, Chungju-si, Chungcheongbuk-do 27469, Republic of Korea

[‡]Authors contributed equally to this study.

ABSTRACT

Conventional computed tomography (CT) uses energy-integrating detectors that cannot resolve spectral differences among co-administered contrast agents (CAs), fundamentally limiting multi-agent discrimination within a single scan. We present a nanoparticle CA-based multiplexed spectral photon-counting CT (SPCCT) framework integrating physics-informed multi-criteria CA elemental selection, nanoparticle-CA synthesis, and multi-material decomposition (MMD) for simultaneous element-specific imaging.

Methods: Contrast elements were selected using physics-informed composite scoring, supplemented by machine learning-based interpretation. Ultrasmall Tb_2O_3 nanoparticles were synthesized and characterized. Multiplex imaging and MMD were evaluated in phantoms and *in vivo*, alongside *in vitro* and *in vivo* biosafety assessment of Tb_2O_3 nanoparticles. Clinical SPCCT evaluation was performed using virtual monoenergetic imaging of CA phantoms.

Results: Iodine (I), terbium (Tb), and gold (Au) were identified as the highest-ranked combination under the evaluated conditions. In phantoms, reference-based MMD assigned each CA to its corresponding channel. Tb_2O_3 nanoparticles of the triad exhibited favorable biosafety in both *in vitro* and *in vivo* assessments. *In vivo* multiplexed SPCCT imaging enabled simultaneous visualization of the three intratumorally administered CAs through reference-based channel assignment, with spatial distribution consistent with the known injection sites. A clinical photon-counting CT system further demonstrated material-dependent contrast trends of the CA triad *via* virtual monoenergetic imaging of phantom models.

Conclusions: These findings support the feasibility of the integrated framework for multiplexed SPCCT imaging under controlled phantom and intratumoral conditions.

KEYWORDS

spectral photon counting computed tomography; contrast agents; multiplexed imaging; physics-informed contrast agent selection; nanoparticles

Introduction

Computed tomography (CT), offering rapid acquisition, high spatial resolution, and broad compatibility with image-guided clinical workflows, has become one of the most widely deployed medical imaging modalities [1]. However, conventional CT measures cumulative X-ray attenuation of all transmitted photons, which limits spectral specificity and the individual contributions of different materials [2]. When multiple contrast agents (CAs) and tissues coexist within the same field of view, their signals are difficult to separate that is a major barrier to multiplexed CT imaging. Dual-energy CT partially addresses this limitation by enabling two-basis material decomposition using different X-ray spectra. However, simultaneous decomposition of three or more independent material components generally requires additional spectral information, assumptions, or constraints [3]. Spectral photon-counting CT (SPCCT) has recently emerged as a next-generation CT platform that overcomes these constraints through energy-resolved photon detection [4]. SPCCT counts individual X-ray photons and assigns them to discrete energy bins, thereby directly measuring the energy-dependent attenuation of different elements [5]. It enables quantitative, voxel-wise, multi-material imaging from a single scan. SPCCT expands the role of CT beyond anatomical imaging toward element-resolved imaging. Recent advances in photon-counting detectors have enabled clinical-grade SPCCT systems, accelerating translation into the clinic and positioning SPCCT as a practical and rapidly evolving imaging modality.

K-edge imaging is one of the key features of SPCCT. As attenuation changes sharply at the K-edge of each element, materials with distinct K-edge energies can generate element-specific spectral signatures when appropriate energy thresholds are applied [6]. This enables multiplexed contrast imaging, in which multiple CAs encode spectral information without temporal misregistration, repeated CA injections, or increased radiation exposure. In this context, CAs act not only as attenuation enhancers but as spectrally distinct labels. Effective SPCCT CAs should have K-edge energies within the clinically accessible energy range, adequate spectral separation to minimize cross-talk, and compatibility with the limited number of energy bins and energy resolution [7, 8]. The success of multiplexed SPCCT imaging depends on the spectral combination of the full CA set, the collective K-edge energy composition, and material decomposition algorithms, rather than on the properties of a single CA alone. Iodine (I), gadolinium (Gd), and gold (Au) are among the most widely studied contrast

elements for SPCCT [9-12]. Iodine-based CAs are routinely used in clinical imaging, and exhibit a sharp increase in attenuation above their K-edge at 33.2 keV, providing strong contrast in the low-energy region of diagnostic X-ray spectrum. Au nanoparticles (NPs) have been extensively studied in preclinical SPCCT because of their high atomic number. Gd-based agents are also clinically available and effective for binary spectral imaging, although spectral considerations constrain their suitability for multiplexed, multi-material SPCCT [13]. At the intermediate energies around the Gd K-edge, attenuation from iodine remains substantial while photon statistics decline. This combination leads to strong spectral covariance and ill-conditioned material decomposition when three or more materials are present [14]. As a result, I-Gd combinations can be suboptimal for robust, high-dimensional SPCCT imaging. These limitations motivate the exploration of alternative mid-*Z* elements with K-edge energies that provide improved spectral orthogonality.

Here, we present an integrated framework for multiplexed SPCCT imaging that combines physics-guided contrast selection with advanced material decomposition. Based on energy-dependent X-ray attenuation characteristics and composite scoring with supplementary machine-learning (ML)-based interpretation, the best CA triad that offers complementary spectral sensitivity with minimal overlap was selected to be an iodine-terbium-gold (I-Tb-Au) CA. This strategy was further implemented by synthesizing terbium oxide (Tb_2O_3) NPs together with a clinically available iodinated small-molecule CA and investigational Au NPs. A custom-assembled photon counting-CT system equipped with an X-ray tube, a cadmium telluride (CdTe)-based photon-counting detector, and a rotatable sample stage was imported to scan our proposed CA triad [15]. Material-resolved SPCCT imaging was achieved using a multi-material decomposition (MMD) algorithm that explicitly exploits the distinct K-edge signatures of each CA, enabling reliable separation of multiple CAs in phantom studies. To support *in viv*o translational development of this spectral contrast element, prerequisite safety assessments of Tb_2O_3 NPs, including *in vitro* cytocompatibility and hemocompatibility profiling alongside *in vivo* tolerability evaluations were performed prior to *in vivo* SPCCT imaging. Then, *in vivo* feasibility of multiplexed SPCCT using the I-Tb_2O_3-Au CA triad was evaluated in a mouse flank tumor model. Intratumoral (*i.t.*) administration of the I-Tb_2O_3-Au CA triad was selected to enable controlled co-localization of CAs and evaluation of multiplexed SPCCT performance *in vivo* physiological imaging conditions. Finally, a comparative SPCCT

contrast effect of I-Tb_2O_3-Au was investigated in the clinical SPCCT scanner. Our work integrating rational K-edge composition, physics-informed contrast selection, safety characterization of an emerging CA, and optimized MMD algorithms establish a scalable approach to multiplexed SPCCT. Potential future applications include integration with nanomedicine and image-guided interventions such as transarterial chemoembolization [16], irreversible electroporation [17, 18], cryoablation [19], and ROS-based cancer therapy [20]. More broadly, this framework provides a generalizable strategy for designing multi-contrast SPCCT systems that integrate detector physics, algorithmic optimization, and CA chemistry.

Results and Discussion

Physics-informed contrast agent triad selection with supplementary ML analysis

True multiplexed SPCCT imaging can be achieved by combining multiple CAs, with imaging performance strongly depending on the rational selection of CA combinations. Reliable material decomposition requires CAs whose energy-dependent attenuation profiles can be distinguished within the available detector bins. In this study, we focused on three CAs combinations to balance the number of contrast channels against spectral separation and photon distribution. Although additional materials can be included in the decomposition model, separating them requires sufficient independent spectral measurements. With a limited number of bins, adding more CAs can increase crosstalk and amplify noise, particularly *in vivo*, where radiation dose and acquisition time constrain photon counts. We therefore compared candidate elemental triads using a multi-criteria framework that accounts for spectral separability and detector constraints (**Figure 1A**). For each candidate element, the effective CT signal contribution was evaluated from its energy-dependent attenuation and the photon spectrum of the X-ray source. Accordingly, the evaluated elements exhibit energy-dependent effective CT signals across the spectrum, reflecting the product of their elemental attenuation profiles and the emitted photon spectrum of a tungsten anode X-ray source (**Figure 1B**) [21]. Specifically, the attenuation term was derived from the energy-dependent mass attenuation coefficient of each element, whereas the X-ray emission spectrum was measured from the tungsten photon source in our SPCCT system. Their product provides a practical estimate of the energy-specific CT signal

contribution relevant to material decomposition. Although Hf, Ta, Au, and Bi exhibited strong cumulative CT signal contributions, much of their attenuation arose from the low-energy portion of the spectrum, resulting in relatively limited signal gain within the post K-edge energy window used for material decomposition (**Figure 1C**). Consequently, these elements show lower self-bin dominance, with greater noise propagation in the decomposed material bins. In contrast, iodine has its K-edge in a region of high photon flux and therefore provides a high self-bin contribution despite its lower atomic number. Substantial attenuation from high-*Z* elements (Ce, Gd, Tb, Yb, Hf, Ta, Au, and Bi) also occurs in this low-energy region, leaving iodine-specific bins susceptible to cross-element signal interference under multi-CA conditions. Gd and Tb occupied a more favorable spectral regime among the evaluated elements: low-energy attenuation was less dominant, while sufficient photons remained available above the K-edges. Their self-bin contributions, noise, and contrast-to-noise ratio (CNR) characteristics were therefore more balanced. These results indicate that each element presents different trade-offs in cumulative signal, bin specificity, and noise behavior during SPCCT-based material decomposition. Selecting CAs with complementary spectral characteristics is thus necessary for robust material separation; K-edge position alone is insufficient.

Inter-element signal crosstalk within each elemental energy bin is an important consideration in MMD. We defined an element-specific energy window starting at the K-edge of each element and normalized the signal contributions of all elements within that window to the target element's K-edge derived signal. Cross-element interference could be compared on the same normalized basis. 9 × 9 normalized mixing matrices with different energy bin widths ranging from 10 to 26 keV are shown in **Figure 1D**, and **Figure S1**. Larger off-diagonal terms were observed for elements with neighboring atomic numbers, indicating greater inter-element signal interference. Wider energy bins led to greater spectral overlap and larger off-diagonal contributions, thereby reducing material separability.

All possible three-element combinations of the candidate elements were compared across a range of energy bin widths selected to account for detector resolution constraints (**Figure 1e**). To assess material separability, we extracted several features from the normalized decomposition matrices, each describing a different aspect of inter-element spectral interactions. These features included self-bin dominance (S_2), pairwise and higher-order inter-

bin coupling (S_3 and S_4), average leakage across bins (L_{mean}), and composite risk metrics that penalizing strong off-diagonal contributions ($RISK_x$). A geometric separability descriptor (D_{geo}) characterized the global distribution of signal contributions across the decomposition space (**Figure S2**). These features were combined in an ML-based scoring framework to rank the triads. Feature importance and SHapley Additive exPlanations (SHAP) analysis indicated that the final score incorporated spectral independence, leakage suppression, and robustness across energy bin widths (**Figure S3**). This approach provided a systemic ranking of CA combinations while retaining an interpretable connection to the underlying physical determinants. The I–Tb–Au triad with an 18 keV energy-bin width ranked highest under the evaluated conditions. This ranking was based on spectral separability and did not include formulation-specific factors such as synthesis feasibility, surface chemistry, elemental loading, or colloidal stability. These factors need to be assessed during contrast-agent development.

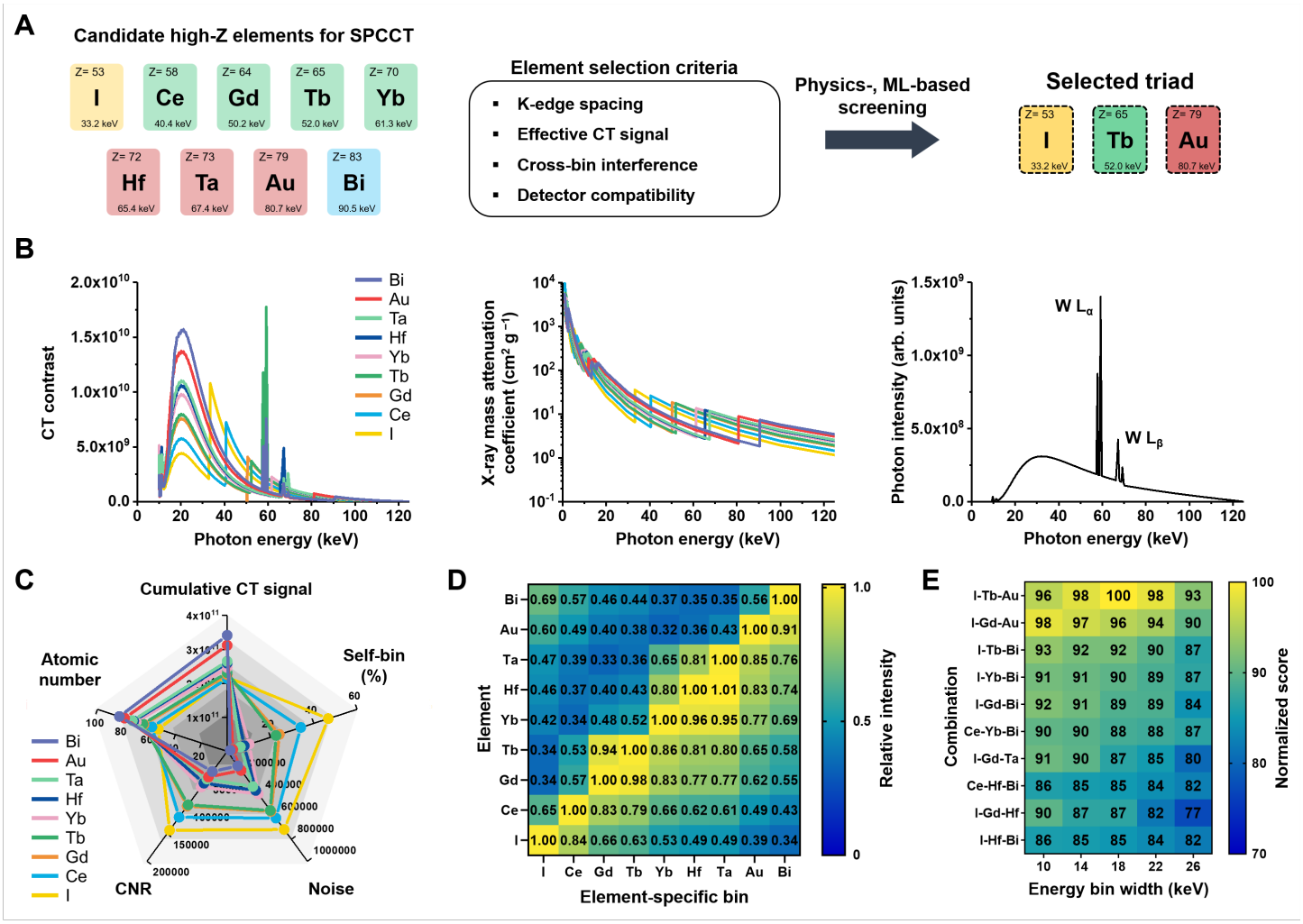


Figure 1. Physics-informed and data-driven framework for selection of contrast element combinations for multiplexed SPCCT. A, Schematic illustration of the multi-criteria element selection used to identify the highest-ranked triad under the evaluated conditions. Candidate elements are color-coded according to their K-edge energy

position, highlighting low-energy (yellow), intermediate-energy (green), and high energy-(red/blue) ranges. **B**, Energy-dependent effective CT signal contributions of candidate contrast elements (left), calculated as the product of elemental attenuation profiles (middle) and the measured X-ray spectrum of the SPCCT photon source across the diagnostic energy range (right). **C**, Radar plot summarizing CT contrast-related metrics of individual candidate elements. **D**, Representative heatmap of normalized inter-element signal contributions, where element-specific bins were defined as fixed 18 keV windows starting at each element's K-edge energy and signal contributions were normalized to the corresponding self-signal (diagonal component). **E**, Composite-score-based ranking of the top 10 element triads evaluated across multiple energy bin widths using matrix-derived factors, with supplementary ML analysis used to interpret the scores. Scores were normalized to a 100-point scale.

Synthesis and characterization of the selected I-Tb_2O_3-Au CAs triad

The intrinsically high metal payloads of NP-based CAs support collective X-ray attenuation with minimal ligand dilution, producing pronounced and stable energy-dependent spectral signatures across SPCCT bins. Metal-based small-molecule CAs typically have lower effective elemental density. The resulting weaker attenuation gradients and greater spectral overlap with background tissue reduce the robustness of multi-component material decomposition. Accordingly, to model a clinically relevant multi-compartment imaging scenario, a contrast agent triad was selected to span distinct pharmacokinetic profiles: a clinically approved iodinated small-molecule CA for rapid vascular and extravascular equilibration, ultrasmall Tb_2O_3 NPs for enhanced interstitial penetration relative to larger nanomaterials, and larger Au NPs for restricted extravasation with prolonged vascular or perivascular retention (**Figure 2A**) [22-26]. The differences in CA size were intended to favor distinct spatial distributions and limit overlap among the agents, rather than ensure complete anatomical separation. When combined with distinct K-edge energies and energy-dependent attenuation characteristics, these coordinated differences were designed to enhance robustness and fidelity of multi-component SPCCT signal separation under realistic imaging conditions. For NP CAs, ultrasmall Tb_2O_3 NPs were synthesized *via* a ligand-assisted precipitation method and subsequently coated with poly(acrylic acid) (PAA), while Au NPs were prepared using a seed-mediated growth method and subsequently functionalized with carboxyl-terminated thiolated polyethylene glycol (HS–PEG–COOH) [19, 27]. Representative transmission electron microscopy (TEM) images show that both Tb_2O_3 NPs and Au NPs possess uniform and well-defined particle morphologies (**Figure 2B**). Quantitative analysis of TEM images showed narrow size distributions for Tb_2O_3 NPs and Au NPs, with average diameters of 3.9 ± 1.1 nm and 31.4 ± 3.1 nm, respectively. Hydrodynamic diameters of Tb_2O_3 and

Au NPs measured by dynamic light scattering (DLS), were 4.7 ± 0.8 nm and 43.5 ± 12.1 nm, respectively (**Figure 2C**). The polydispersity indices of 0.03 for Tb_2O_3 NPs and 0.08 for Au NPs indicate highly monodisperse NP morphologies, suggesting minimal NP aggregation in aqueous dispersion. Both NP formulations had negatively charged surfaces, with zeta potentials of −22.0 ± 12.3 mV and −20.1 ± 14.7 mV, respectively (**Figure 2D**). Fourier transform infrared spectroscopy confirmed the presence of surface carboxyl ligands, accounting for their negative surface charges and aqueous dispersibility (**Figure S4**). Given the comparatively limited use of Tb_2O_3 NPs in biomedical imaging, we examined their structural and chemical properties. High-resolution TEM analysis showed clear lattice fringes corresponding to the (222) plane of cubic Tb_2O_3, indicating the presence of short-range crystalline order at the nanoscale (**Figure 2E**). The small NP size resulted in broadened X-ray diffraction features without sharp reflections, nevertheless, the lattice fringes and corresponding fast Fourier transform patterns confirmed the crystalline oxide structure of the Tb_2O_3 NPs (**Figure S5**). Under ultraviolet excitation, Tb_2O_3 NPs exhibited characteristic 4*f*-related green fluorescence, consistent with their oxide electronic structure (**Figure S5C**). The oxidation state of Tb_2O_3 NPs was examined by X-ray photoelectron spectroscopy (XPS) (**Figure 2F**). The Tb 3*d* spectrum revealed the coexistence of Tb^{3+} and Tb^{4+} valence states, which can be attributed to the high specific surface area of Tb_2O_3 NPs and the associated surface defects (**Figure 2G**). The dispersion stability of Tb_2O_3 NPs was evaluated by DLS analysis following 7 days of storage at 4°C in water, phosphate-buffered saline (PBS), serum-free Dulbecco's modified Eagle's medium (DMEM), and DMEM supplemented with 10% fetal bovine serum (FBS) (**Figure S6**). Gaussian fitting of the size distribution yielded mean hydrodynamic sizes of 5.4, 6.5, 6.6 and 7.2 nm, respectively. These results support good colloidal stability of Tb_2O_3 NPs under the tested media without noticeable aggregation or sedimentation.

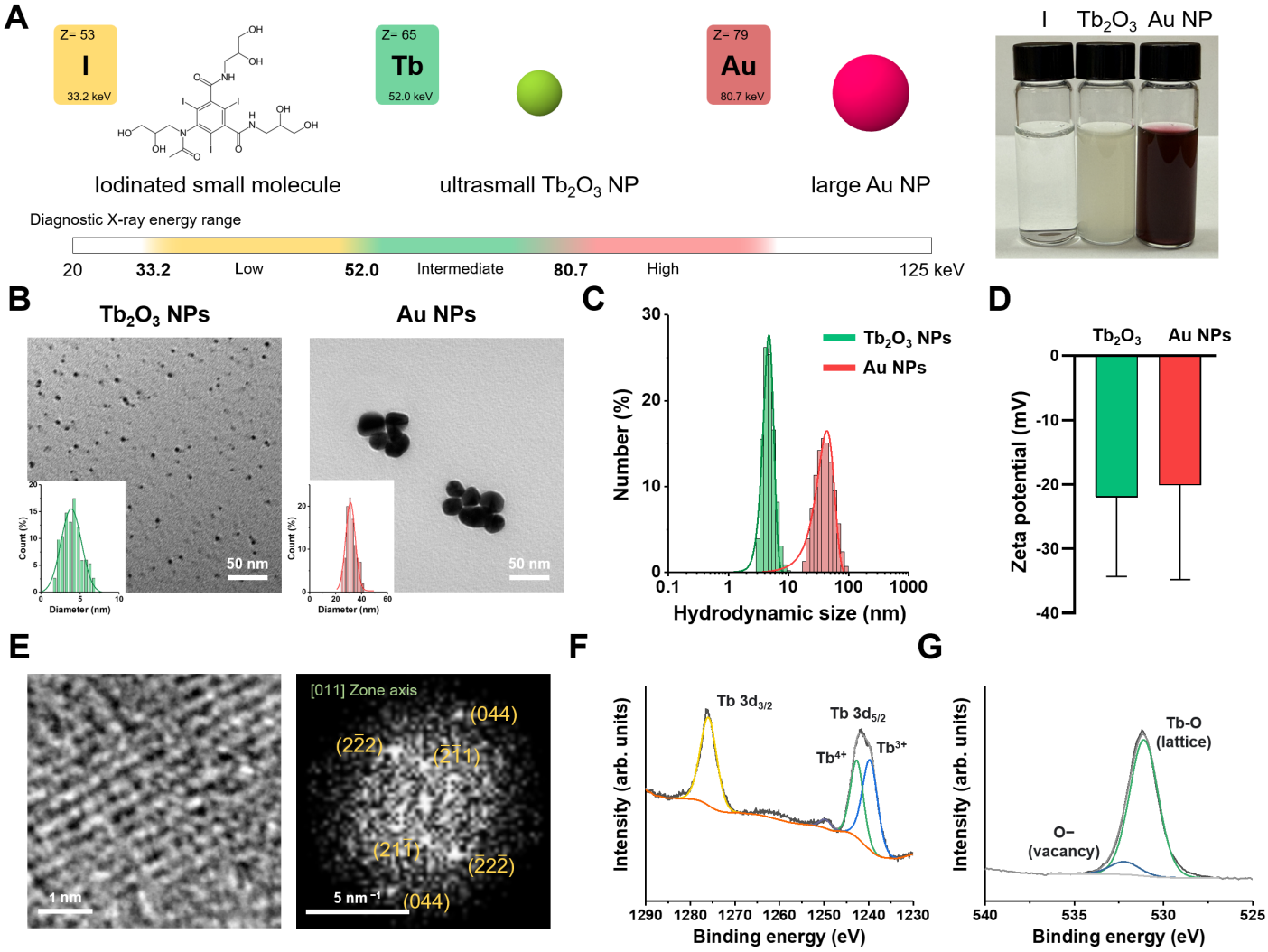


Figure 2. Synthesis and characterization of CAs used for SPCCT imaging. A, Schematic diagram illustrating the I-Tb-Au triad CA system, consisting of an iodinated small-molecule CA, ultrasmall Tb_2O_3 NPs, and Au NPs. Digital photograph of iodinated small-molecule CA, Tb_2O_3 NPs, and Au NPs prepared at the same elemental concentration (5 mg element mL^{-1}), illustrating their intrinsically different formulations and colloidal appearances. **B**, Representative TEM image of ultrasmall Tb_2O_3 NPs and larger Au NPs. Insets show the corresponding particle size distributions obtained from TEM analysis with diameters measured for n = 1000 Tb_2O_3 NPs and n = 100 Au NPs, respectively. Scale bars indicate 50 nm. **C-D**, hydrodynamic size distribution (C) and zeta potential (D) of Tb_2O_3 NPs and Au NPs in deionized water using DLS. **E**, High-resolution TEM image, and FFT patterns of Tb_2O_3 NPs. **F-G**, Tb 3*d* (F), and O 1*s* (G) XPS spectrum of Tb_2O_3 NPs.

Energy bin-resolved SPCCT signal characterization and multi-material decomposition

Unlike conventional energy-integrating CT, which integrates attenuation across the full detected spectrum (Total energy range; TE), or dual-energy CT, whose broad low- and high-energy bands lack the spectral granularity to resolve element-specific K-edge features, SPCCT enables flexible energy binning that aligns photon count acquisition directly with the K-edge energies of targeted contrast agents. The three prepared CAs were evaluated for separated CT signal responses using CA-specific energy bins in the custom-assembled SPCCT

(**Figure 3A**). Based on the optimized 18 keV bin width (**Figure 1E**), the detected photon spectrum was divided into I-, Tb-, and Au-oriented bins defined relative to their respective K-edge energies (**Figure 3B**). Representative SPCCT images demonstrate distinct bin-dependent signal distributions for each CA (**Figure 3C**), while full concentration-dependent datasets are provided in **Figure S7** and **Figure S8**. Quantitative analysis of bin-specific CT signal intensities revealed differential response patterns across the CA-oriented bins (**Figure 3D**). Linear regression of CT signal intensity as a function of CA concentration was performed for each bin to extract bin-specific slopes, which quantify effective contrast sensitivity within the defined energy bins. Each CA exhibited the highest contrast sensitivity in its corresponding CA-oriented bin, with substantially reduced sensitivities observed in non-corresponding bins, indicating limited cross-bin signal contribution at the signal acquisition level. These results establish the feasibility of CA-oriented signal separation using SPCCT and provide the quantitative basis for subsequent material decomposition using algorithmic approaches.

Material decomposition in photon-counting CT is typically formulated as an image-domain inverse problem that relates energy-resolved attenuation measurements to material basis functions. To resolve individual CA contributions from the multi-energy attenuation data, we performed MMD using constrained iterative optimization using single-CA phantoms as a controlled benchmark (**Figure 3E**). Briefly, the energy-dependent linear attenuation measured in each spectral bin was modeled as a linear combination of material-specific spectral responses, and the resulting inverse problem was solved using sparsity-regularized iterative optimization to recover individual volume fractions. This benchmark assessed whether material decomposition correctly assigned each CA's attenuation signal to its corresponding material channel. TE images provide limited material specificity, whereas application of the MMD framework enabled reconstruction of CA-specific images corresponding to iodine, Tb, and Au (**Figure 3F**). In single-CA phantoms, the reconstructed images were dominated by the target CA with minimal interference from other materials. Crosstalk analysis of the single-CA phantoms showed that MMD assigned most of the reconstructed VF to the corresponding material channel, with little signal in the other channels (**Figure 3G**).

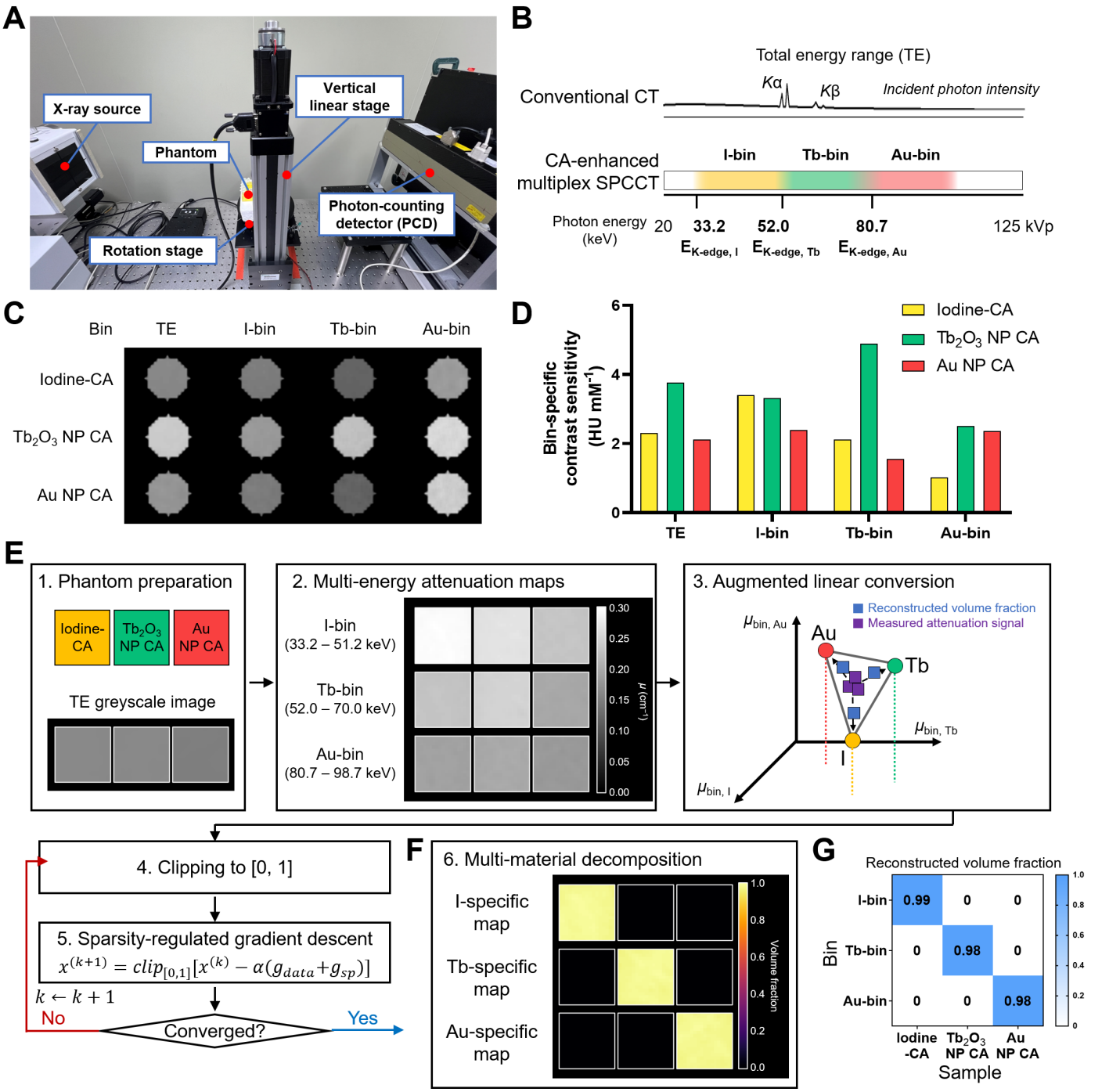


Figure 3. Contrast-agent-oriented energy-resolved CT signal characterization. A, Photograph of the custom-assembled SPCCT system, highlighting the photon-counting detector used for multiplex energy acquisition. **B**, Schematic illustration of the energy bin configuration used for CA-oriented SPCCT imaging. **C**, Representative SPCCT phantom slice images acquired at a fixed CA concentration, demonstrating distinct attenuation responses of each CA across different energy bins. **D**, Bin-specific contrast sensitivity of individual CAs, quantified from linear fits of HU as a function of elemental concentration (I, Tb or Au; mM) for each energy bin. **E**, Illustration of the phantom imaging and MMD algorithm workflow. The phantom included single-CA samples containing iodine, Tb_2O_3, and Au with elemental concentrations of 85.0, 25.6, and 13.7 mM for I, Tb, and Au, respectively. A representative image reconstructed over the total energy range is shown, followed by CA-specific K-edge images reconstructed at corresponding CA-oriented energy bins. These energy-resolved images were processed using the MMD algorithm with iterative optimization to generate CA-specific decomposition maps. **F**, Final MMD-reconstructed images oriented to each CA. Color scales show volume fraction (VF), the dimensionless

decomposition coefficient (0−1). **G**, Quantitative cross-talk analysis based on the ROI-mean VF in the single-agent samples, shown as a cross-talk matrix summarizing residual inter-material leakage after MMD.

Biosafety profile of ultrasmall Tb_2O_3 nanoparticles

Although iodinated small-molecule agents are clinically established and the biocompatibility of Au NPs is well documented, the biosafety profile of lanthanide oxide-based Tb_2O_3 NPs remains incompletely defined [28-30]. We therefore conducted a stepwise translational safety evaluation encompassing cytocompatibility, hemocompatibility, innate immune activation, and *in vivo* tissue tolerance (**Figure 4A** and **Table S1**). Toxicity evaluations were designed to reflect biological interfaces most relevant to administered CAs, focusing on cell types that would be directly exposed to Tb_2O_3 NPs, including tumor cells, tumor-associated vascular endothelium, and circulating immune cells. Time and dose dependent cellular responses to Tb_2O_3 NPs were investigated in three different cell types including RAW264.7 macrophages, SK-BR-3 breast cancer cells, and HUVEC endothelial cells. The three-dimensional surface plots showed a gradual decline in metabolic activity with increasing Tb_2O_3 NPs concentration and incubation time, with no abrupt cytotoxic threshold evident in any of the three cell types (**Figure 4B**). Dose-response analyses at 24 h further showed that RAW264.7 and HUVEC cells retained >80% viability up to 2 mg mL^{-1}, whereas SK-BR-3 cells maintained comparable viability up to 0.5 mg mL^{-1}, followed by a gentle concentration-dependent decline at higher doses (**Figure 4C**). These findings indicate low *in vitro* cytotoxicity toward endothelial and immune cells over the tested concentration ranges. Hemocompatibility was assessed since administered CAs come into contact with blood during circulation and tissue perfusion. Annexin V staining revealed no increase in leukocyte apoptosis after NP exposure at 5 or 10 mg mL^{-1} at any tested incubation time (**Figure 4D**). The $CD61^+$ platelet assay showed no significant difference in the measured response compared with controls. No visible hemolysis, aggregation, or sedimentation was observed after whole-blood exposure over the tested concentration range (**Figure 4E**). Quantitative measurements confirmed negligible hemolysis at concentrations relevant to SPCCT administration. Serum C3a levels remained unchanged across NP concentrations, suggesting no detectable increase in complement activation under the tested conditions (**Figure 4F**). For the *in vivo* assessment, the liver, spleen, kidneys, lungs, and heart were collected 7 days after *i.t.* NP injection for histological examination. Tissue architecture was preserved, with no apparent

inflammation, necrosis, hemorrhage, or vascular injury relative to the phosphate-buffered saline control (**Figure 4G**). Blood Tb levels and tissue distribution were evaluated following intravenous (*i.v.*) and *i.t.* administration of Tb_2O_3 NPs in mice bearing subcutaneous prostate cancer (TrampC1) in the flank (**Figure S9**). Mean blood Tb levels were lower in the *i.t.* group than in the *i.v.* group at all measured time points (1, 7, and 14 days after injection). At day 14, tissue Tb contents were highest in the liver and kidney in the *i.v.* group, whereas the tumor showed the highest Tb content in the *i.t.* group. This distribution pattern confirmed tumor retention of Tb_2O_3 NPs at day 14 following *i.t.* injection, whereas *i.v.* administration led to preferential accumulation in organs involved in the processing and elimination of circulating substances. Body weight remained relatively stable in both *i.v.* and *i.t.* groups over two weeks observation period, supporting tolerability under the tested conditions. No significant differences in body weight change or tumor growth were observed between the treatment and control groups over the 14-day observation period. The long-term fate of lanthanide oxide NPs depends on particle size, surface chemistry, and biological transformation. Renal clearance has been demonstrated for certain ultrasmall NPs, including specific Gd oxide formulations, whereas other lanthanide oxide formulations exhibit prolonged tissue retention and slower hepatobiliary eliminations [23, 31, 32]. In the present study, hepatic and splenic Tb retention at day 14 after *i.v.* administration may reflect uptake by the reticuloendothelial system. Retained lanthanide oxides may also undergo dissolution and phosphate-mediated transformation within acidic lysosomal compartments, processes that have been linked to lysosomal injury in experimental rare-earth oxide systems [33, 34]. Although the present assessments support tolerability over the evaluated observation period, longer-term tissue measurements, urinary and fecal analysis, and assessment of hepatic, renal, and inflammatory responses are needed to establish the persistence, elimination, and delayed safety effects of Tb_2O_3 NPs.

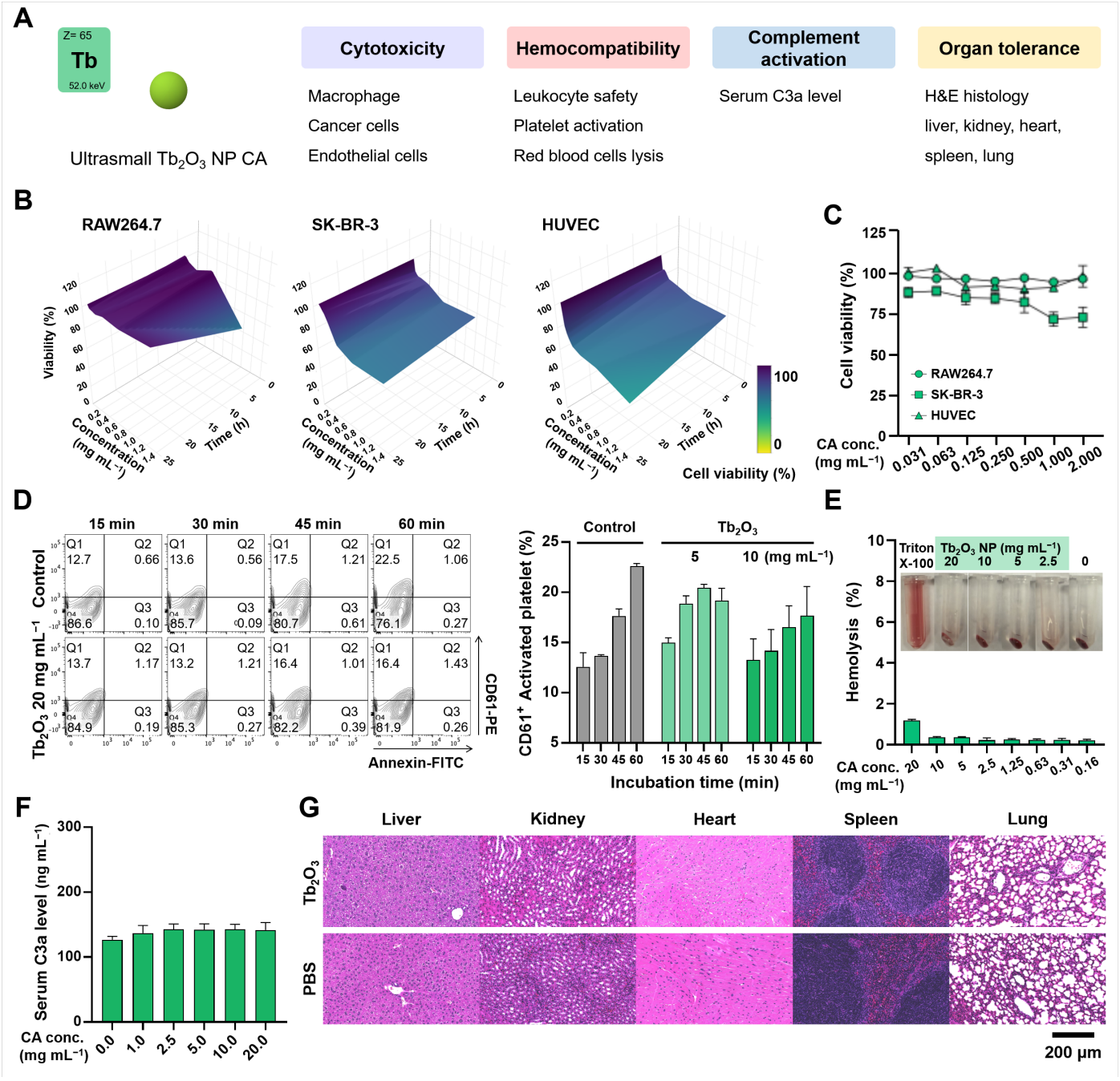


Figure 4. Biosafety assessment of ultrasmall Tb_2O_3 NPs for SPCCT CA applications. A, Schematic overview of the biosafety evaluation of ultrasmall Tb_2O_3 NP CA. **B**, Surface plots showing viability of RAW264.7, SK-BR-3, and HUVEC cells depending on the Tb_2O_3 NPs concentration and incubation time. **C**, Dose-dependent viability of RAW264.7, SK-BR-3, and HUVEC cells 24 h after Tb_2O_3 NP treatment. **D**, Annexin staining of leukocytes at the indicated time points following NP incubation, and $CD61^+$ platelet activation after incubation with Tb_2O_3 NP CA (5 and 10 mg mL^{-1}). **E**, Hemolysis assay after the treatment with different concentrations of Tb_2O_3 NPs. **F**, Serum C3a levels following *in vitro* incubation of rat blood with Tb_2O_3 NPs at the indicated concentrations. **G**, H&E-stained images of main organs (liver, kidney, heart, spleen, and lung) 7 days after *i.t.* injection of Tb_2O_3 NPs.

In vivo multiplexed SPCCT imaging

In vivo multiplexed SPCCT imaging of the I-Tb_2O_3-Au NP CA triad was performed in a bilateral flank tumor model established by subcutaneous implantation of EO771 murine breast cancer cells in C57BL/6N mice (**Figure 5A**). SPCCT scans were performed sequentially at pre- and post-infusion of Tb_2O_3 NPs and Au NPs in each right and left tumor, respectively. Then, iodinated CA was injected into both tumors, enabling stepwise evaluation of multi-contrast imaging (**Figure 5B**). Greyscale CT images reconstructed at the total energy range showed increased attenuation at both injected tumor sites after CAs administration (**Figure 5C**). However, these greyscale images did not provide material-specific information and could not distinguish the contribution of the individual CAs. To examine element-enhanced contrast before material decomposition, K-edge imaging focused on the characteristic absorption edges of iodine, Tb, and Au revealed CA-dependent contrast modulation *in vivo* (**Figure 5D**). These K-edge images showed contrast modulation associated with each selected energy window, but signal contributions from multiple CAs remained mixed within each bin. As a result, K-edge imaging alone was insufficient for unambiguous localization and selective identification of each administered CA under multi-contrast conditions. Material decomposition was applied to resolve the spatial distribution of each CA *in vivo* (**Figure 5E**). In contrast to the mixed signal contributions observed in the K-edge bin images, the decomposed maps enabled CA-specific visualization within contrast-enhanced regions defined by an attenuation mask. Tb_2O_3 NP signal was selectively localized to the right tumor, Au NP signal to the left tumor, and iodine signal to both injection sites. This spatial specificity indicates effective reduction of inter-element signal interference and improved assignment of decomposed signals to their corresponding CAs under multiplexed *in vivo* conditions. The composite overlay image further highlighted the spatial coexistence and relative distribution of the three CAs within the tumor microenvironment. The decomposed maps agreed with the known injection sites. In a second mouse, the same procedure with an animal-specific two-component reference matrix assigned Tb and Au VFs to their injection sites (**Figure S10**). In two additional mice, focal enhancement was observed at the injection sites in the corresponding K-edge bin images. Quantitative analysis yielded CNRs of 13.3 and 20.4 for Tb_2O_3 NPs in mice 3 and 4, respectively, and 8.3 for Au NPs in mouse 4 (**Figure S10F**). These results demonstrate that the proposed SPCCT-based strategy extends element-enhanced K-edge imaging to multiplex CT imaging with multiple CAs. We note that the VFs reported here are reference-based decomposition coefficients that reflect

relative material specificity rather than absolute elemental concentration. As complementary evidence, ICP-MS analysis in a separate biodistribution cohort showed a tumor Tb content of 55.6 ± 22.4 %ID/g at 14 days following intratumoral administration of Tb_2O_3 NPs (mean ± SD, n = 4; **Figure S9**). These measurements quantify tumor-associated Tb following local administration, but differences in tumor models and animal cohorts prevent their use as direct validation of the imaging-derived VFs. Matched *ex vivo* elemental analysis of the imaged tumors was not performed; the relationship between VF and intratumoral elemental content therefore remains to be established in a larger, standardized cohort. The decomposition is limited by the inclusion of local background in the reference responses, meaning that the VFs represent reference-based channel assignments within the specified masks rather than calibrated concentrations. Tissue with attenuation characteristics that differ from those of the reference regions may therefore contribute to the contrast-agent channels. Quantitative elemental imaging will require explicit background modeling, concentration calibration, and ex vivo validation in larger cohorts. With only three energy bins, incorporating an additional background component will require additional energy bins or constraints.

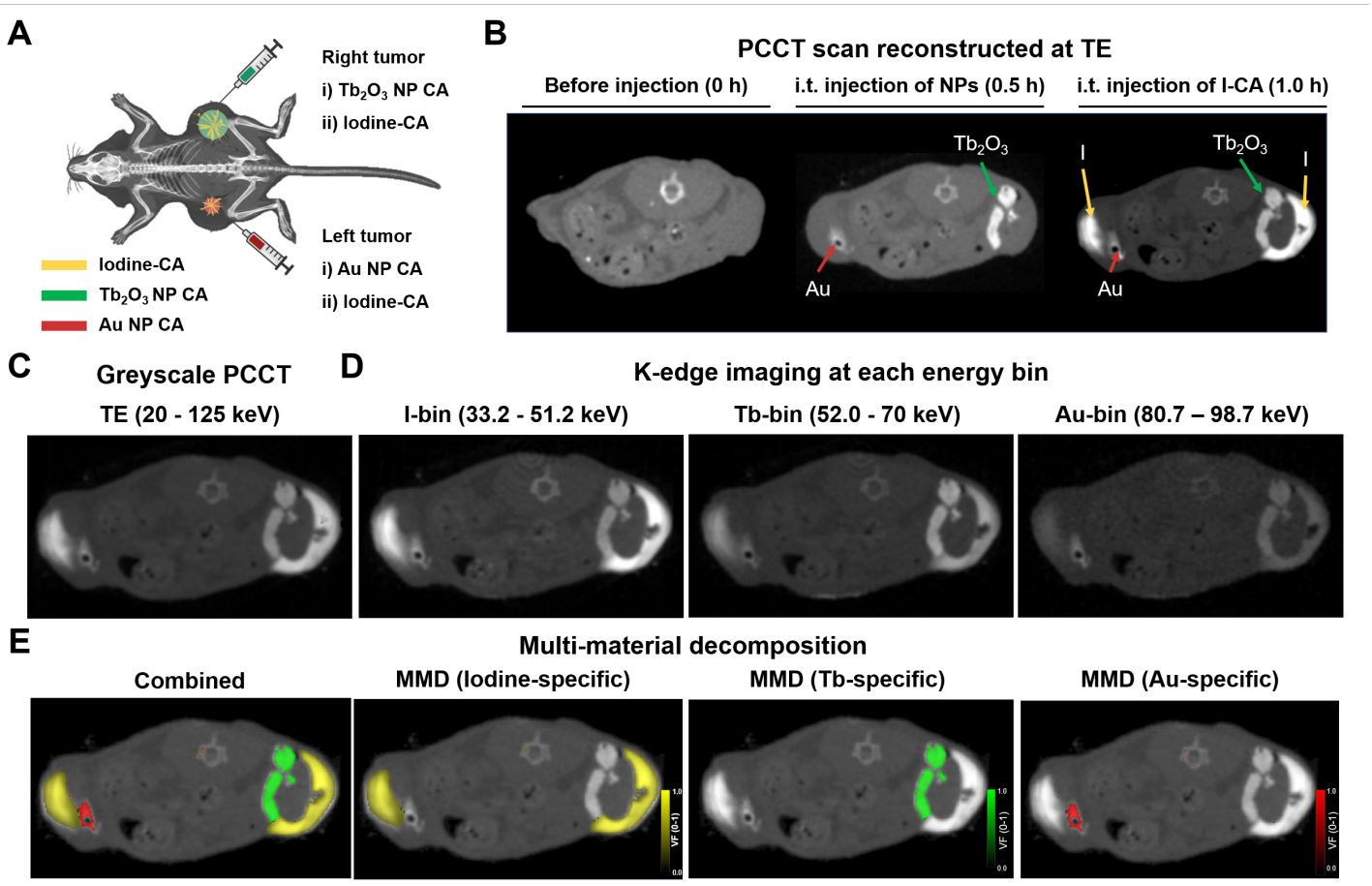


Figure 5. *In vivo* multiplex SPCCT imaging and material decomposition of the I-Tb_2O_3-Au triad CAs. A, Schematic illustration of the *in vivo* experimental design, showing serial *i.t.* administration of CAs. **B**, PCCT images acquired during the sequential CA administration: pre-injection baseline image (left), image after intratumoral (*i.t.*) injection of Au NPs and Tb_2O_3 NPs into the left and right tumors, respectively (middle), and image after subsequent *i.t.* administration of iodine CA into both sites (right). Arrows indicate the location of Au, Tb_2O_3, and iodine CA. **C**, Representative *in vivo* PCCT image reconstructed over the entire energy range. **D**, Representative K-edge bin images reconstructed at the element-specific energy bins corresponding to each CA. **E**, Multi-material decomposition images for each CA, demonstrating selective identification of iodine, Tb_2O_3, and Au *in vivo*. Color scales show VF, the dimensionless decomposition coefficient (0−1); overlays show VF above 0.15 within the analysis mask.

Clinical SPCCT evaluation of the I-Tb_2O_3-Au triad

Validating these findings on a clinical SPCCT platform represents the next translational step, yet translation from a custom benchtop setup is constrained by limited energy bin flexibility, restricted access to projection-domain raw data, and proprietary reconstruction pipelines - factors compounded by the lower photon flux and smaller field of view inherent to benchtop systems, which may alter noise characteristics and spectral overlap behavior relative to whole-body clinical scanners. Under these acquisition constraints, virtual monoenergetic imaging (VMI) is used to reconstruct CT images at selected monoenergetic levels from the measured spectral dataset. Although VMI does not provide direct material decomposition, it offers an energy-specific representation of reconstructed contrast and can be used to characterize material-dependent attenuation behavior on the clinical platform [35]. To characterize the material-dependent attenuation and contrast behavior of the I-Tb_2O_3-Au NP CA triad under clinical acquisition conditions, agarose-embedded phantoms containing each agent individually and in combination were scanned on a Siemens NAEOTOM Alpha SPCCT system using a standard clinical protocol (**Figure 6A**). VMI images reconstructed at 40, 52, and 81 keV showed material-dependent contrast sensitivity, and linear fitting confirmed differential attenuation slopes for iodine-CA, Tb_2O_3 NP, and Au NP across the reconstructed VMIs (**Figure 6B**). Although the overall trends were similar across reconstructions, the slope differences provide measurable contrast separation that can be leveraged for multi-CA imaging under clinical settings. Importantly, VMI differences alone do not constitute material decomposition; rather, they demonstrate material-dependent contrast behavior in the clinical VMI workflow, and their implications for three material decomposition remain to be established. Representative single-CA phantom images illustrated reconstruction-dependent contrast differences for iodine-CA, Tb_2O_3 NP, and Au NP across TE and VMI conditions (**Figure 6C**,

and **Figure S11**). This confirms that CA-specific attenuation characteristics are preserved under imaging conditions of a clinical scanner, despite differences in photon flux, detector pixel size, and energy threshold configuration between custom-assembled and clinical SPCCT systems (**Figure S12**). We evaluated the material-dependent contrast behavior of the CA triad using a combined phantom consisting of an iodine-CA dispersed agarose matrix with spatially separated Tb_2O_3, Au inserts and an air reference (**Figure 6D**). In the combined phantom, the iodine-containing background and the embedded Tb_2O_3 NP and Au NP inserts remained differentially represented across TE and VMI reconstructions, indicating that the relative attenuation behavior of the three contrast agents was preserved under clinical imaging conditions. CNR analysis further confirmed reconstruction-dependent differences in insert conspicuity across the VMI datasets (**Figure 6E**). Because the clinical evaluation was restricted to attenuation profiling using vendor-provided VMI rather than direct multi-material decomposition, these results should be interpreted as evidence of preserved material-dependent attenuation behavior rather than absolute quantitative elemental separation. Image-based decomposition of iodine, gadolinium, and water has been demonstrated on a clinical NAEOTOM Alpha scanner using a four-threshold research mode and system-specific calibration [36]. The proposed MMD framework likewise operates in the image domain, providing a basis for extension to clinical SPCCT when suitable energy-resolved images and system-specific calibration are available. However, implementation and validation of three-agent MMD for the I–Tb–Au combination on clinical platforms remain objectives for future works.

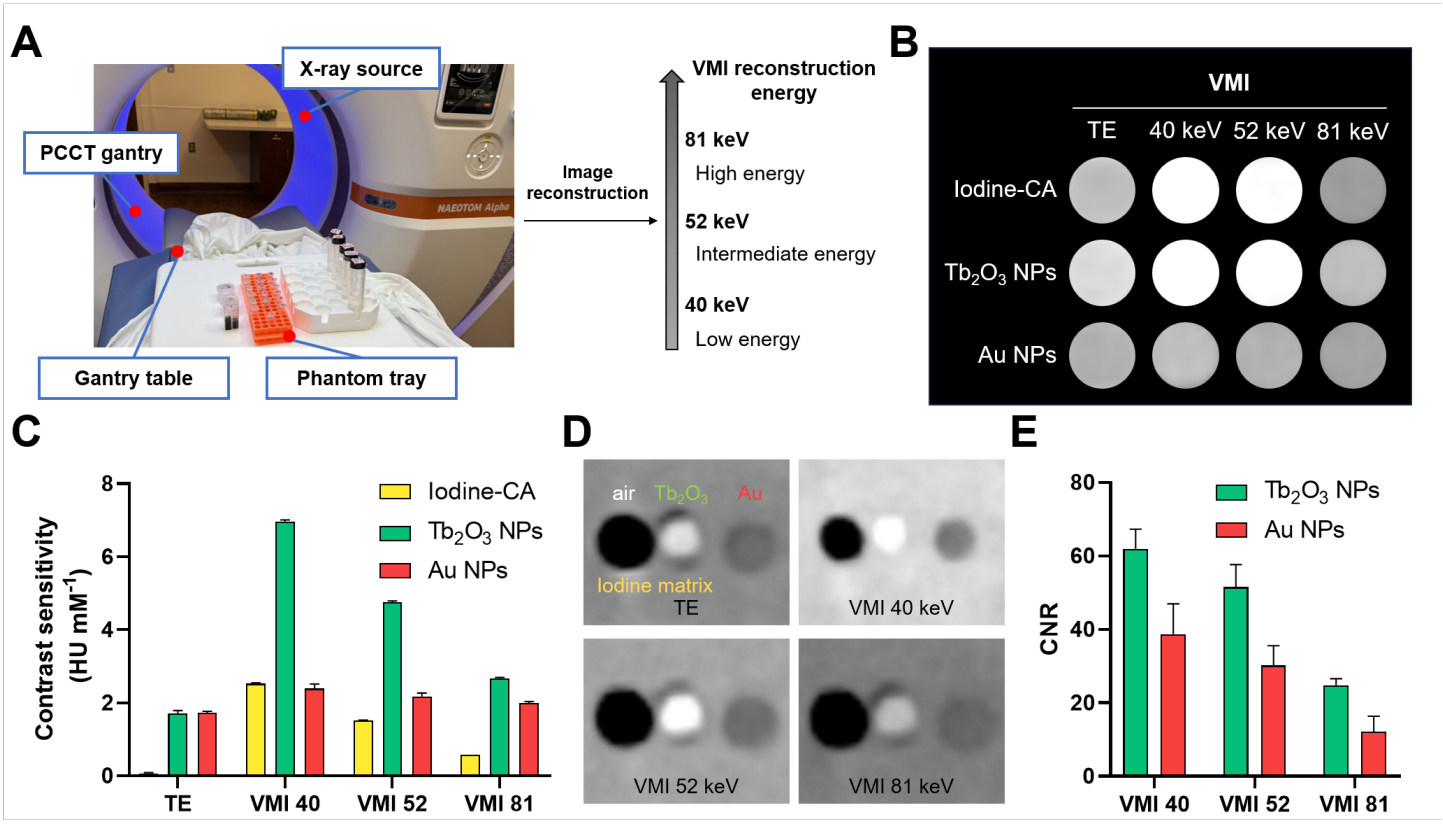


Figure 6. Translational feasibility of the I-Tb_2O_3-Au CA triad on a clinical SPCCT scanner. A, Photograph of the agarose-embedded multi-contrast phantom positioned on a clinical photon-counting CT system (NAEOTOM Alpha, Siemens Healthineers), and a schematic summary of the selected virtual monoenergetic image (VMI) levels used in this study. **B**, Representative TE and VMI images of single-CA phantoms containing iodine, Tb_2O_3 NPs, and Au NPs at elemental concentrations of 170.0, 51.2, and 54.6 mM for I, Tb, and Au, respectively, based on the principal contrast elements. **C**, Concentration-dependent CT response of iodine, Tb_2O_3 NPs, and Au NPs, summarized as reconstruction-specific contrast sensitivity defined as the linear fitted attenuation slope (HU mM^{-1}) from total energy (TE) reconstruction and VMI at 40, 52, and 81 keV. Linear fitting was performed using five concentration levels for each CA, with five independent slices analyzed per concentration. **D**, TE and VMI images of a combined phantom prepared separately from the single-CA phantoms in B. Tb_2O_3 NPs and Au NPs were separately mixed with agarose in tubes. These tubes and an air-filled reference tube containing neither agarose nor CA, were embedded in an iodine-containing agarose matrix. The iodine matrix, the Tb_2O_3 NP insert, and Au NP insert had elemental concentration of 17.0, 25.6, and 13.7 mM, respectively. **E**, CNR values of the Tb_2O_3 NP and Au NP inserts measured from the VMI with an iodine-matrix background.

Conclusion

This study demonstrates a systematic framework for multiplexed SPCCT CA design, suggesting a new approach beyond atomic-number-driven selection toward quantitatively optimized, clinically adaptable multi-CA configurations. By evaluating candidate CA triads across detector-constrained energy bin widths using composite scoring, the I–Tb–Au triad with an 18 keV bin width was successfully identified as the highest-ranked combination under the evaluated detector energy-bin configuration. Supplementary ML analysis was used to

interpret the resulting scores. Reference-based multi-material decomposition assigned each CA to its channel in phantoms and localized the three CAs to their injection sites *in vivo*. Finally, clinical phantom imaging demonstrated energy-dependent attenuation profiles of the CA triad within the vendor-provided VMI workflow. Further translational development of the CA triad and multiplexed SPCCT imaging will require collaboration with scanner manufacturers to enable research acquisition modes, adjustable energy thresholds, and reconstruction pipelines that support multi-material decomposition. Additionally, NP-based K-edge CAs are well suited for surface functionalization in multiplexed molecular imaging, where targeting moieties such as antibodies or peptides can direct CA accumulation to specific tissues, and improve diagnostic specificity. This capability would advance SPCCT beyond anatomical toward simultaneous multi-target molecular quantification within a single acquisition. Therefore, strong interdisciplinary partnership harmonizing CA design with detector architecture and MMD algorithm development is foundational to transitioning multiplexed SPCCT from proof-of-concept to a standardized platform for next-generation precision diagnostics and image-guided therapeutics.

Methods

Physics-driven quantitative evaluation of SPCCT candidate elements

The energy-dependent mass attenuation coefficients $\mu\ \rho(E)^{-1}$ of each element were obtained from the NIST Standard Reference Database 126 [21]. The incident X-ray spectrum $S(E)$ was measured under the experimental SPCCT conditions using a tungsten-filament source operated at 125 kVp and 100 mA (RAD-14, Varian Medical Systems, UT). The tabulated mass attenuation coefficients were interpolated to match the energy grid of the incident spectrum. The effective energy-resolved CT contrast was calculated as $I(E) = S(E)\cdot\mu\ \rho(E)^{-1}$, combining each element's mass attenuation coefficient with the measured photon spectrum. The cumulative CT signal for element i was defined as $\int I_i(E)dE$, to compare the elements under the same acquisition conditions. This modeling enabled direct comparison of element-specific attenuation behavior under identical SPCCT conditions. Element-specific energy bins were defined as windows starting at the K-edge energy of each candidate element and extending over a fixed bin width. Bin-wise responses were obtained by integrating $I_i(E)$ over each window. This procedure yielded an element-bin response matrix Q, where each entry Q_{ik} represents the normalized response of element i in bin k and the absolute sensitivity of element i is represented by the diagonal term M_{ii} of the absolute sensitivity matrix M_{abs}. The signal contribution of element i in bin k was defined as $S_{i,k} = M_{ii}Q_{ik}$. Noise variance in bin k was approximated assuming Poisson-dominated photon-counting statistics and expressed as $\sigma_k^2 \propto \sum_j M_{jj}Q_{ik}$. Proportionally constants associated with radiation dose, detector gain, voxel size, and reconstruction scaling were omitted because the acquisition conditions were held constant across comparisons. To quantify contrast between a target element i and a background material b in the same energy bin, the contrast-to-noise ratio (CNR) was defined as $CNR_{i,b,k} = |M_{ii}Q_{ik} - M_{bb}Q_{bb}|/(\sum_j M_{jj}Q_{jk})^{1/2}$. This approximation assumes measurements within the same energy bin and neglects covariance terms between the element and background signals. The background material was defined as water. Spectral cross-talk was quantified using the self-bin contribution, defined as the fraction of the total signal in a given bin originating from the target element: $\text{Self-bin}_i(\%) = (S_{i,k}/\sum_i S_{i,k}) \times 100$.

Data-driven composite scoring of triad performance across energy bin widths

For multi-element combinational evaluation, multiple acquisition scenarios s were defined by varying ΔE, the post K-edge integration window W. To enable relative comparison across elements and bins, the response matrix was normalized so that the diagonal elements were unity ($Q_{ii} = 1$), corresponding to the primary bin of each element. Off-diagonal terms therefore represent relative cross-bin responses arising from spectral overlap. With this normalization, the diagonal sensitivity matrix retains each element's absolute sensitivity, while Q describes relative bin mixing and cross-talk. A full 9 × 9 response matrix was constructed for the nine candidate elements across the defined energy bins. This matrix summarizes element-bin responses under the specified acquisition conditions and was used for correlation analysis and triad selection. To evaluate the feasibility of simultaneous three-element imaging, all possible element triads were enumerated from the candidate set. For each triad, a reduced 3 × 3 response submatrix A was extracted from the full 9 × 9 matrix by selecting the rows and columns corresponding to the three elements and their respective bins. From each triad matrix, multiple complementary performance metrics were calculated. Pairwise separability ($S2$) was quantified as $S2 = 1 - \max_{i \neq j} A_{ij}$, penalizing the strongest cross-bin coupling. Volumetric separability ($S3$) was evaluated using the determinant $S3 = \det(A)$, and its logarithm was used for numerical stability. Conditioning and inversion robustness ($S4$) were quantified as $S4 = \sigma_{min}\ \sigma_{max}^{-1}$, where σ_{min} and σ_{max} denote the minimum and maximum singular values of submatrix. Spectral leakage was quantified using the total off-diagonal sum $L_{total} = \sum_{i \neq j} A_{ij}$, $L_{mean} = L_{total}/6$. Worst-case directional instability was characterized by $R_{\max} = \max_j \sum_{j \neq i} A_{ij}$, $C_{\max} = \max_j \sum_{i \neq j} A_{ij}$, from which risk metrics were derived with geometric mean as $RISKx = (R_{\max} \cdot C_{\max})^{0.5}\ 2^{-1}$. Triad-level detectability was quantified using the geometric mean $D_{geo} = (M_{aa}^{(s)} M_{bb}^{(s)} M_{cc}^{(s)})^{1/3}$, together with the minimum diagonal sensitivity D_{min}. For each triad and energy bin width (W: 10, 14, 18, 22, 26 keV), six quantitative metrics were computed ($S2$, $S3$, $S4$, L_{mean}, $RISK_X$, and D_{geo}). Because these metrics differ in scale and optimal direction, they were first transformed such that larger values consistently represented better performance. $S2$, $S4$, and D_{geo} were used directly, whereas $S3$ and $RISK_X$ were converted using $f(x) = 1 - |x - 1|$, and L_{mean} was negated so that smaller values corresponded to larger scores. Each transformed feature was then standardized across all samples using z-score normalization. A composite performance score was calculated for every triad-W pair as the equally weighted sum of the standardized features, reflecting the absence of prior evidence favoring any single feature. To characterize overall performance

regardless of bin width W, composite scores were aggregated by triad to obtain the mean value across the full W range, and triads were additionally ranked within each W to determine the number of first-place occurrences. For interpretability, the mean composite score of each triad was further linearly rescaled to a 0-100 range using min-max normalization, which preserves the relative ranking while providing an intuitive performance scale. All analyses were implemented in Python using pandas and scikit-learn. To further investigate the relative contributions of individual performance metrics to the composite ranking, a RF model was used as a complementary ML-based interpretability analysis. The six standardized performance metrics ($S2$, $S3$, $S4$, L_{mean}, $RISK_X$, and D_{geo}) were used as input features with the composite performance score as the prediction target. Two analyses were conducted: a triad-level analysis using metrics aggregated across all energy bin widths and a bin-specific analysis restricted to W = 18 keV. Feature importance was quantified using the RF model, and SHAP were applied to characterize the contributions of individual metrics to the model predictions. These analyses were intended to interpret the relative influence of the predefined scoring criteria rather than to independently optimize or validate triad performance. Accordingly, candidate triad selection was based on the physics-informed composite scoring framework, whereas RF and SHAP were used exclusively for supplementary model interpretation.

Synthesis and characterization of NP-based CAs

For the synthesis of small Tb_2O_3 NPs, 2 mmol of terbium acetate hydrate ($Tb(CH_3CO_2)_3 \cdot xH_2O$, Sigma-Aldrich, MO, USA) and 3 mmol of L-cysteine ($HSCH_2CH(NH_2)CO_2H$, Sigma-Aldrich, MO, USA) were added into 20 mL of dimethyl sulfoxide ($(CH_3)_2SO$, Sigma-Aldrich, MO, USA) and mixed solution heated up to 65^{o}C for 2 h to dissolve precursors using a silicon oil bath. Then, 1 mL of tetramethylammonium hydroxide ($(CH_3)_4N(OH)$, Sigma-Aldrich, MO, US) was added into the solution and kept heated for 2 h. During this step, the color of the solution gradually changed from milk to pale lemon. Then 3 mmol of polyacrylic acid was added into the mixture and the final solution was stirred for 12 h using a magnetic bar. Au NPs were prepared by a seed-mediated growth method. Citrate-stabilized seeds (approximately 10 nm) were grown to the target size by incremental addition of 20 mM $HAuCl_4$ and 60 mM trisodium citrate under magnetic stirring. Au NP was functionalized with HS-

PEG3.4k-COOH (HE003017-3.4k, Biopharma PEG, MA, USA) for 24 h. Both NPs were centrifuged and purified with H_2O for 5 times to remove free precursors and surfactants. Final NPs were dispersed in deionized water (Millipore Direct-Q UV3) at 4°C. Morphology and size of NPs were evaluated by transmission electron microscopy (TEM; FEI Tecnai Spirit G2, FEI Company, OR, USA) and aberration-corrected TEM (JEOL ARM200CF, JEOL Ltd. Japan). Hydrodynamic diameter and zeta potential were measured by dynamic light scattering (DLS, Zetasizer Nano ZS90, Malvern Panalytical, UK) in H_2O at pH 7.4. For dispersion stability assessment, freshly synthesized Tb_2O_3 NPs were transferred into water, PBS, serum-free DMEM, or DMEM supplemented with 10% FBS and stored at 4°C for 7 days. Following storage, hydrodynamic size distributions were measured by DLS at 25°C. The distributions were fitted with Gaussian functions to determine the peak hydrodynamic diameters. Surface composition and valence state were probed by X-ray photoelectron spectroscopy (XPS, NEXSA G2, ThermoFisher Scientific, MA, USA) and elemental quantification was performed by inductively coupled plasma mass spectrometry (ICP-MS, iCapQ, Thermo, MA, USA) after digestion in acid.

Phantom preparations

Serial dilutions of each CA were prepared at defined concentration ranges. An iodinated CA (Omnipaque™ (iohexol), 300 mg I mL^{-1}, GE Healthcare, IL, USA) was diluted to concentrations of 0-43.1 mg mL^{-1}, while Tb_2O_3 and Au NP solution were prepared at concentrations ranging from 0-20.0 mg mL^{-1}. All samples were embedded in 1% (*w/v*) agarose gels and stored at 4°C.

Custom-assembled photon counting-CT and data acquisition

Spectral CT imaging was performed using a benchtop photon-counting CT system consisting of an X-ray tube (RAD-14, Varian Medical Systems, UT, USA), a cadmium telluride (CdTe)-based photon-counting detector (XC-TDI, Varex Imaging, UT, USA), and a rotatable sample stage. The detector has a pixel size of 100 μm and an array size of 3584 × 60 pixels, corresponding to an active detection area of 360 × 6 mm^2. It was operated in photon-counting mode with a linear array configuration, allowing the incident X-ray spectrum to be divided into

multiple energy bins. During image acquisition, the sample was rotated while the X-ray source and detector remained fixed. Reconstruction was performed using a GPU-accelerated Feldkamp-Davis-Kress (FDK) algorithm [15, 37]. This photon-counting CT system has been previously described and validated for quantitative spectral imaging applications [15]. The CdTe-based detector was selected for its high photoelectric absorption efficiency across the diagnostic energy range, allowing efficient X-ray detection with a thinner sensor than lower-Z materials such as silicon [1, 38-40]. Both CdTe and cadmium zinc telluride (CZT) are high-*Z* direct-conversion semiconductors commonly used in photon-counting CT. CdTe is also used in custom-assembled systems because of its fabrication characteristics and established detector array configurations [39, 40]. Charge sharing between adjacent pixels and K-fluorescence escape can reduce spectral fidelity in these detectors, particularly at small pixel pitches [38]. The 100 μm pixel pitch of the XC-TDI detector represents a trade-off between high spatial resolution and charge-sharing effects. At the photon flux used in this benchtop system, pulse pile-up was limited, allowing energy discrimination across the acquisition bins [38, 39]. Although this system differs from clinical whole-body SPCCT scanners in geometry, flux, and field of view, its flexible energy threshold placement and multi-energy bin capability provide a controlled platform for validating material decomposition algorithms [1]. In the present study, the tube was operated at 125 kVp and 4 mA without additional filtration, and 1,440 projections were acquired over 360° at a detector frame rate of 12 Hz. For material decomposition, a separate acquisition was performed in which element-specific energy bins were defined on the basis of the K-edge energies of each contrast agent (I: 33.2 keV, Tb: 52.0 keV, Au: 80.7 keV) with fixed width of 18 keV, thereby capturing element-resolved attenuation signatures. Detector data were 4 × 4 binned prior to reconstruction, yielding a reconstructed voxel size of 0.4 × 0.4 × 0.2 mm^3.

Multi-material decomposition

In SPCCT, the detector records photon counts in discrete energy bins. Each energy bin captures X-ray attenuation from all materials present in the imaging volume, weighted by their energy-dependent mass attenuation coefficients. To recover the contribution of each CA, the measured attenuation is expressed as a linear forward model: $\mu(E_b) = \sum_m^M F_{b,m} \cdot x_m$ (**Eq. 1**), where $\mu(E_b)$ is the measured linear attenuation coefficient in energy bin b,

$F_{b,m}$ is the spectral response coefficient of material m in bin b, x_m denotes the volume fraction (VF) of material m, defined here as a dimensionless decomposition coefficient relative to the measured reference response rather than a physical VF, and M corresponds to the number of materials. Each column of F was measured in a reference region in which the corresponding CA predominated (single-agent agarose samples in the phantom study and in situ regions in each animal in the *in vivo* studies), so each reference response includes the attenuation of its surrounding matrix or tissue (Supporting Information Note 1). In physical terms, each energy bin records a composite signal in which every material's contribution is proportional to both its intrinsic X-ray absorption characteristics and its local concentration. As each CA exhibits distinct K-edge energies, the spectral response matrix F encodes CA-specific attenuation profiles that enable their separation. Recovering the unknown volume fractions x from the measured attenuation μ therefore constitutes an inverse problem given a mixture signal, the algorithm must determine how much of each material is present. Non-enhanced tissue was not modeled as a separate component; analyses were restricted to attenuation masks (phantom: iodine-bin or Tb-bin attenuation above 0.15 cm^{-1}; mouse 1 (Figure 5): iodine-bin attenuation above 0.40 cm^{-1}; mouse 2 (**Figure S10**): Tb-bin or Au-bin attenuation above the body mean + 1.5 SD), voxels outside the masks were set to zero, and objects outside the body were masked in the displayed images. An initial estimate was obtained by direct inversion of the response matrix, or by least squares for the two-component (Tb, Au) analysis of mouse 2, in which iodine was administered intravenously; initial values were clipped to [0, 1] for the phantom and set to zero outside [0, 2] for the *in vivo* data, and no unity-sum constraint was imposed. However, direct inversion alone is sensitive to noise and spectral overlap between materials, which can produce spurious cross-talk between decomposition bins. To suppress these artifacts, the initial estimate was iteratively refined using a sparsity-regularized gradient descent that exploits the physical prior that most voxels contain only a small number of materials. For instance, a voxel located within an iodine-enhanced region should have near-zero volume fractions for terbium and gold. At each iteration, the volume fractions were updated using the gradient of the data-fidelity and nonconvex l_{p-norm} sparsity terms ($p < 1$), followed by clipping to [0, 1]. The algorithm parameters were determined empirically for each dataset; iterations stopped when the absolute change in the data-fidelity term fell below a tolerance or at the maximum number of iterations. The complete mathematical derivation, including the iterative update rule and stopping

criteria, is provided in **Supporting Information Note 1**, with the pseudocode summarized in Algorithm 1 and the pipeline illustrated in **Figure S13**.

Quantification of cross-talk

A crosstalk leakage index was defined using single-material phantoms. For each target material x, the diagonal response was defined as the recovered volume fraction (VF) in its own bin k, $D_k = VF_{k\to k}$. The total off-diagonal leakage was calculated as the sum of recovered volume fraction in non-target bins j: $O_k = \sum_{j\neq k} VF_{k\to j}$. The crosstalk leakage was then identified as the normalized leakage ratio: $Leakage_k = O_k\, D_k^{-1}$.

Cell lines and culture

RAW264.7 (mouse macrophage, TIB-71), SK-BR-3 (human breast adenocarcinoma, HTB-30), and human umbilical vein endothelial cells (HUVEC, CRL-1730) were sourced from the American Type Culture Collection (ATCC, VA, USA). The murine breast carcinoma cell line EO771 (C57BL/6 origin) was obtained from CH3 BioSystems (Amherst, NY, USA). RAW264.7 and EO771 cells were grown in Dulbecco's Modified Eagle's Medium (DMEM; Gibco, USA), while SK-BR-3 cells were maintained in McCoy's 5A medium (Gibco, Thermo Fisher Scientific, MA, USA). All media were supplemented with 10% (v/v) heat-inactivated fetal bovine serum (FBS; Gibco, USA) and 1% (v/v) penicillin-streptomycin solution. HUVECs were cultured in EBM®-Plus basal endothelial cell growth medium supplemented with the BulletKit® additives (CC-5035; Lonza, MD, USA), according to the manufacturer's instructions. All cells were incubated at 37°C under humidified 5% CO_2 and routinely passaged every 1-2 days or before reaching approximately 80% confluence. For passaging, adherent cells were detached using 0.25% (w/v) trypsin-EDTA solution (Gibco).

Animals

All animal experimental procedures were reviewed and approved by the Institutional Animal Care and Use Committee (IACUC) of Northwestern University and the Korea Advanced Institute of Science and Technology (KAIST), depending on the study. Male C57BL/6 mice (5-6 weeks old, 18-20 g; Charles River Laboratories, MA,

USA) were used under approved IACUC protocol (IS00002377). Sprague-Dawley rats (male, 8-10 weeks, 300-400 g; Charles River Laboratories, MA, USA) were utilized under approved IACUC protocol (IS00008540). Female C57BL/6N mice (5 weeks old; Koatech, Pyeongtaek, Republic of Korea) were maintained under specific pathogen-free conditions at the Laboratory Animal Resource Center of KAIST (Daejeon, Republic of Korea) under an approved IACUC protocol (KA2025-007-v1).

Biocompatibility of Tb_2O_3 NPs

The cytotoxicity of Tb_2O_3 NPs was evaluated using RAW264.7, SK-BR-3, and HUVEC cell lines. Cells were seeded at a density of 1×10^4 cells per well and incubated with various concentrations of Tb_2O_3 NP for 4 or 24 h. After incubation, cells were rinsed three times with Dulbecco's Phosphate Buffered Saline (DPBS; Corning, NY, USA). Cell viability was evaluated using CCK-8 reagent (Dojindo, Japan) and detected at 450 nm using a Synergy HT spectrophotometer (BioTek, VT, USA). Three-dimensional surface plots depicting cell viability as a function of incubation time and concentration were generated using R software in RStudio (R Foundation, Vienna, Austria). Platelet activation induced by Tb_2O_3 NPs was evaluated using whole blood collected from Sprague-Dawley rats. Blood samples were collected into tubes containing 3.2% sodium citrate. The anticoagulated blood was incubated with Tb_2O_3 NPs at various concentrations (2.5, 10, and 20 mg mL^{-1}) for 1 h under gentle agitation. Following incubation, platelets were stained with PE-conjugated anti-CD61 antibody (1:200, BD Science, CA, USA) and FITC-conjugated Annexin V (ab14085, Abcam, Cambridge, UK). Platelet activation was analyzed by flow cytometry using a BD Fortessa system (BD Biosciences, CA, USA). Hemocompatibility was further assessed by a hemolysis assay. Whole blood from C57BL/6 mice was collected and red blood cells were isolated by centrifugation and washed with isotonic saline. The erythrocytes were then incubated with Tb_2O_3 NPs at various concentrations for 1 h at 37°C. After incubation, samples were centrifuged and the absorbance of the supernatant was measured to quantify released hemoglobin. Hemolysis percentages were calculated relative to negative (DPBS) and positive (1% (v/v) Triton X-100 solution) controls. To evaluate the immunological safety of the Tb_2O_3 NPs, complement activation was assessed by quantifying complement component C3 levels in rat serum. Whole blood samples were incubated with Tb_2O_3 NPs at concentrations of 1, 2.5, 5, 10, and 20 mg mL^{-1}

for 1 h. The samples were then centrifuged to obtain serum, and aliquots were analyzed using a rat Complement C3a ELISA kit (NBP270039, Novus Biologicals™, CO, USA) according to the manufacturer's instructions. Serum C3a concentrations were calculated based on a standard curve generated using known C3a standards. To evaluate the *in vivo* biocompatibility of Tb_2O_3 NPs, a flank tumor model was established using TrampC1 murine prostate cancer cells in male C57BL/6 mice. Tumor cells were subcutaneously implanted into the flank region, and Tb_2O_3 NPs were administered *via i.t.* injection after tumors reached the designated size. At predetermined time points following NP administration, major organs including the heart, lung, liver, kidney, and spleen were harvested and fixed in 4% paraformaldehyde solution. Then, 5 μm-thick issue sections were stained with hematoxylin and eosin. All slides were scanned using a Nanozoomer 2.0-HT slide scanner (Hamamatsu, Shizuoka, Japan).

***In vivo* SPCCT imaging**

To establish the subcutaneous tumor models, 1.0×10^6 EO771 cells in serum-free DMEM were injected into both the left and right flanks of five-week-old female C57BL/6N mice under anesthesia ($n = 5$). Tumor volumes (V) were measured using calipers and calculated as $V = (W^2 \times L) \times 0.5$; W: width, L: length. Once the tumors reached approximately 200 mm^3, animals were randomly assigned into experimental groups to ensure comparable baseline tumor sizes. For *i.t.* administration, 20 μL of each agent was injected into the tumors immediately prior to imaging at final concentrations of 54 mg mL^{-1} (Au), 40 mg mL^{-1} (Tb), and 80 mg mL^{-1} (I_2, dry-mass equivalent). In mouse 1, Tb_2O_3 and Au NPs were administered intratumorally into the right and left tumors, respectively, followed by intratumoral administration of iodine into both tumors. Mouse 2 also received intratumoral Tb_2O_3 and Au NPs at separate tumor sites. Images from mice 1 and 2 were processed using the MMD-AP algorithm (**Figure 5** and **Figure S10A–E**). Mice 3 and 4 contained Tb_2O_3 NPs alone or Tb_2O_3 and Au NPs, respectively, within the imaged volume. These animals were imaged using two K-edge bins each: I- and Tb-bins for mouse 3, and Tb- and Au-bins for mouse 4. Because these acquisition configurations were not evaluated in the phantom decomposition study, mice 3 and 4 were included in SNR/CNR analysis but not material decomposition. Mouse 5 received intravenous iodine and intratumoral Tb_2O_3 and Au NPs before euthanasia,

followed by freezing and transport. This animal was excluded from the quantitative comparison because of the different sample preparation conditions. SNR and CNR were measured in the corresponding K-edge bin images using 5 × 5-pixel ROIs at the injection sites in mice 1–4 (**Supporting Information Note 1, S4**). Background pixels were selected within the body region, at least 3 pixels from its boundary. Exclusion masks were defined using the analysis masks for mice 1 and 2 and pixels exceeding the body-region mean intensity by 1.5 SD in an acquired K-edge bin for mice 3 and 4. Each exclusion mask was dilated by 3 pixels before background selection. Sensitivity to ROI placement was assessed in mice 3 and 4 by shifting the ROIs by one pixel and recalculating CNR.

Clinical SPCCT imaging and VMI-based contrast characterization

Clinical photon-counting CT imaging was performed on a whole-body photon-counting CT scanner (NAEOTOM Alpha, Siemens Healthineers). All scans were acquired at 140 kVp using a tungsten anode X-ray source and detector-based spectral acquisition. Vendor-provided reconstructions generated from the same acquisition included total energy (TE) images, and virtual monoenergetic images (VMI) at 40, 52, and 81 keV. Two distinct phantom configurations were used. Single-CA samples were prepared in microtubes for individual-agent imaging and concentration-dependent analysis (**Figure 6B–C**). For combined-phantom imaging, Tb_2O_3 NPs and Au NPs were separately mixed with agarose in PCR tubes and embedded in an iodine-containing agarose matrix together with an air reference (**Figure 6D–E**). The iodine matrix had an elemental concentration of 17.0 mM I. Each NP insert contained 5.0 mg mL^{-1} of nanoparticles, expressed as total nanoparticle mass including the inorganic and organic components. Based on ICP-MS measurements of elemental content, these concentrations corresponded to 25.6 mM Tb and 13.7 mM Au, respectively. All concentrations expressed in mM refer to the contrast-generating elements I, Tb, and Au.

ASSOCIATED CONTENT

Supporting Information Available:

Supporting note and figures: Multi-Material Decomposition Algorithm; Physics-driven normalized decomposition matrices for candidate contrast elements; Triad-level response matrices and metric decomposition; Feature-level interpretation of composite scoring using supplementary ML analysis; Surface and structural characterization of Tb_2O_3 NPs; Concentration-dependent CT number in each CA; Elemental concentration-based CT number in each CA; Blood kinetics, tissue distribution, and 14-day monitoring following administration of Tb_2O_3 NPs in mice bearing TRAMP-C1 tumors; Combined CA phantom images using the preclinical SPCCT; In vivo SPCCT imaging and K-edge material decomposition in a second mouse.

AUTHOR INFORMATION

Corresponding Author

[*]Dong-Hyun Kim - *Department of Radiology, Feinberg School of Medicine, Northwestern University, Chicago, IL 60611, USA; Robert H. Lurie Comprehensive Cancer Center, Northwestern University, Chicago, IL 60611, USA; Department of Biomedical Engineering, McCormick School of Engineering, Northwestern University, Evanston, IL 60208, USA; Department of Biomedical Engineering, University of Illinois, Chicago, IL 60607, USA;* Email: dhkim@northwestern.edu

Present Addresses

[+]Min Jun Ko - *School of Materials Science and Engineering, Kumoh National Institute of Technology, Gumi-si, Gyeongsangbuk-do 39177, Republic of Korea*

[++]Sanghee Lee - *School of Nanomedical Engineering, Korea National University of Transportation, Chungju-si, Chungcheongbuk-do 27469, Republic of Korea*

Author Contributions

‡M.J.K. and ‡K.S. contributed equally to this work. M.J.K., K.S., and D.H.K. conceived project and designed the project; M.J.K., K.S., and S.L. performed the experiments and analyzed the data; J.H.H and M.A assisted with the experiments, data curation, and data analysis; A.A.B., A.C.G., and R.J.L. provided professional support and suggestions for SPCCT studies; M.J.K., K.S., and D.H.K. wrote the initial draft. All authors contributed to the writing of the final manuscript. D.H.K. supervised the overall research.

Data and materials availability

The Python scripts used for the machine learning-based ranking analysis in this study are publicly available on GitHub (https://github.com/BIGMedLab/SPCCT-MultiElement). The raw benchtop projection data are available from the corresponding author upon reasonable request, subject to approval under ETRI's institutional data-sharing procedures. The implementation code for the MMD algorithm is not publicly distributed in view of an existing technology transfer agreement.

Declaration of Competing Interest

Amir A. Borhani reports institutional research support, travel support, and honoraria from Siemens Healthineers.

Abbreviations

CT, computed tomography; CA, contrast agent; SPCCT, spectral photon-counting CT; I, iodine; Gd, gadolinium; Au, gold; NP, nanoparticle; ML, machine learning; CNR, contrast to noise ratio; Tb_2O_3, terbium oxide; CdTe, cadmium telluride; MMD, multi-material decomposition; SHAP, SHapley Additive exPlanations; TEM, transmission electron microscopy; DLS, dynamic light scattering; XPS, X-ray photoelectron spectroscopy; TE, Total energy range; DE-CT, Dual-energy CT; VMI, virtual monoenergetic imaging; VF, volume fraction

Acknowledgements

This work was supported by National Cancer Institute (NCI) grants (R01CA282664, R01CA278956 and R01CA279040). The Lurie Cancer Center is supported in part by an NCI Cancer Center Support Grant (NCI P30 CA060553). K.S acknowledges the support by internal fund of Electronics and Telecommunications Research Institute (ETRI): [25YR1610].

AI declaration

During the preparation of this manuscript, the authors used AI-assisted tool (OpenAI and Anthropic Claude) for language polishing to improve the clarity and readability.

References

1. Willemink MJ, Persson M, Pourmorteza A, Pelc NJ, Fleischmann D. Photon-counting CT: technical principles and clinical prospects. Radiology. 2018; 289: 293-312.
2. Greffier J, Viry A, Robert A, Khorsi M, Si-Mohamed S. Photon-counting CT systems: a technical review of current clinical possibilities. Diagn Interv Imaging. 2025; 106: 53-9.
3. Alvarez RE, Macovski A. Energy-selective reconstructions in x-ray computerised tomography. Phys Med Biol. 1976; 21: 733-44.
4. van der Bie J, van Straten M, Booij R, Bos D, Dijkshoorn ML, Hirsch A, et al. Photon-counting CT: review of initial clinical results. Eur J Radiol. 2023; 163: 110829.
5. McCollough CH, Rajendran K, Leng S, Yu L, Fletcher JG, Stierstorfer K, et al. The technical development of photon-counting detector CT. Eur Radiol. 2023; 33: 5321-30.
6. Gunaseelan N, Saha P, Maher N, Pan D. Nanoparticles with “K-edge” metals bring “color” in multiscale spectral photon counting X-ray imaging. ACS Nano. 2024; 18: 34464-91.
7. Douek PC, Boccalini S, Oei EH, Cormode DP, Pourmorteza A, Boussel L, et al. Clinical applications of photon-counting CT: a review of pioneer studies and a glimpse into the future. Radiology. 2023; 309: e222432.
8. Jost G, McDermott M, Gutjahr R, Nowak T, Schmidt B, Pietsch H. New contrast media for K-edge imaging with photon-counting detector CT. Invest Radiol. 2023; 58: 515-22.
9. Kim J, Bar-Ness D, Si-Mohamed S, Coulon P, Blevis I, Douek P, et al. Assessment of candidate elements for development of spectral photon-counting CT specific contrast agents. Sci Rep. 2018; 8: 12119.
10. Balegamire J, Vandamme M, Chereul E, Si-Mohamed S, Maache SA, Almouazen E, et al. Iodinated polymer nanoparticles as contrast agent for spectral photon counting computed tomography. Biomater Sci. 2020; 8: 5715-28.
11. Dong YC, Hajfathalian M, Maidment PS, Hsu JC, Naha PC, Si-Mohamed S, et al. Effect of gold nanoparticle size on their properties as contrast agents for computed tomography. Sci Rep. 2019; 9: 14912.
12. Gil CJ, Evans CJ, Li L, Allphin AJ, Tomov ML, Jin L, et al. Leveraging 3D bioprinting and photon-counting computed tomography to enable noninvasive quantitative tracking of multifunctional tissue engineered constructs. Adv Healthc Mater. 2023; 12: 2302271.
13. Si-Mohamed S, Bar-Ness D, Sigovan M, Tatard-Leitman V, Cormode DP, Naha PC, et al. Multicolour imaging with spectral photon-counting CT: a phantom study. Eur Radiol Exp. 2018; 2: 34.

14. Sawall S, Baader E, Trapp P, Kachelrieß M. CT material decomposition with contrast agents: single or multiple spectral photon-counting CT scans? A simulation study. Med Phys. 2025; 52: 2167-90.
15. Son K, Kim D. Deep learning estimation of effective atomic number for HU to RED calibration in dual energy photon counting CT. Sci Rep. 2026; 16(1): 3604.
16. Kim H, Choi B, Mouli SK, Choi H, Harris KR, Kulik LM, et al. Preclinical development and validation of translational temperature sensitive iodized oil emulsion mediated transcatheter arterial chemo-immuno-embolization for the treatment of hepatocellular carcinoma. Adv Healthc Mater. 2023; 12: 2300906.
17. Han JH, Lee YY, Shin HE, Han J, Kang JM, Wang C-PJ, et al. Image-guided in situ cancer vaccination with combination of multi-functional nano-adjuvant and an irreversible electroporation technique. Biomaterials. 2022; 289: 121762.
18. Lee S, Kim S, Yu ES, Lee S, Ko MJ, Lee H, et al. Electric pulse regulated MXene based nanozymes for integrative bioelectricity immuno-cancer therapy. Adv Funct Mater. 2025; 35: 2420870.
19. Ko MJ, Lee S, Jeon YS, Kim DH. Dynamic fractal ice nano-nucleators for cancer cryotherapy. Nano Today. 2024; 59: 102501.
20. Ko MJ, Kim S, Han JH, Lee S, Ahn M, Fu HE, et al. MXene wrapped magnetic mesocrystals for durable redox catalytic cancer therapy and responsive MRI. Adv Funct Mater. 2026; 36: e76343.
21. Hubbell JH, Seltzer SM. Tables of X-ray mass attenuation coefficients and mass energy-absorption coefficients 1 keV to 20 MeV for elements Z= 1 to 92 and 48 additional substances of dosimetric interest. National Inst. of Standards and Technology-PL, Gaithersburg, MD: National Institute of Standards and Technology; 1995. Report No.: NISTIR 5632.
22. Lusic H, Grinstaff MW. X-ray-computed tomography contrast agents. Chem Rev. 2013; 113: 1641-66.
23. Choi HS, Liu W, Misra P, Tanaka E, Zimmer JP, Itty Ipe B, et al. Renal clearance of quantum dots. Nat Biotechnol. 2007; 25: 1165-70.
24. Epple M, Rotello VM, Dawson K. The why and how of ultrasmall nanoparticles. Acc Chem Res. 2023; 56: 3369-78.
25. Rosario-Berríos DN, Pang A, Liu LP, Maidment PS, Kim J, Yoon S, et al. The effect of the size of gold nanoparticle contrast agents on CT imaging of the gastrointestinal tract and inflammatory bowel disease. Bioconjug Chem. 2025; 36: 233-44.
26. Chen W, Wang W, Xie Z, Centurion F, Sun B, Paterson DJ, et al. Size-dependent penetration of nanoparticles in tumor spheroids: a multidimensional and quantitative study of transcellular and paracellular pathways. Small. 2024; 20: 2304693.
27. Tegafaw T, Liu Y, Ho SL, Liu S, Ahmad MY, Al Saidi AKA, et al. High-quantum-yield ultrasmall Ln2O3 (Ln = Eu, Tb, or Dy) nanoparticle colloids in aqueous media obtained via photosensitization. Langmuir. 2023; 39: 15338-42.
28. Zhang R, Kiessling F, Lammers T, Pallares RM. Clinical translation of gold nanoparticles. Drug Deliv Transl Res. 2023; 13: 378-85.
29. Najjar R. Clinical applications, safety profiles, and future developments of contrast agents in modern radiology: a comprehensive review. iRadiology. 2024; 2: 430-68.
30. Luo Z, Yi Z, Liu X. Surface engineering of lanthanide nanoparticles for oncotherapy. Acc Chem Res. 2023; 56: 425-39.
31. Kryza D, Taleb J, Janier M, Marmuse L, Miladi I, Bonazza P, et al. Biodistribution study of nanometric hybrid gadolinium oxide particles as a multimodal SPECT/MR/optical imaging and theragnostic agent. Bioconjug Chem. 2011; 22: 1145-52.
32. Tian X, Yang F, Yang C, Peng Y, Chen D, Zhu J, et al. Toxicity evaluation of Gd2O3@SiO2 nanoparticles prepared by laser ablation in liquid as MRI contrast agents in vivo. Int J Nanomedicine. 2014; 9: 4043-53.
33. Li R, Ji Z, Chang CH, Dunphy DR, Cai X, Meng H, et al. Surface interactions with compartmentalized cellular phosphates explain rare earth oxide nanoparticle hazard and provide opportunities for safer design. ACS Nano. 2014; 8: 1771-83.
34. Tian M, Wu D, Gou X, Li R, Zhang X. Genetic modulation of rare earth nanoparticle biotransformation shapes biological outcomes. Nat Commun. 2025; 16: 3429.
35. D'Angelo T, Cicero G, Mazziotti S, Ascenti G, Albrecht MH, Martin SS, et al. Dual energy computed tomography virtual monoenergetic imaging: technique and clinical applications. Br J Radiol. 2019; 92: 20180546.

36. Treb KJ, Marsh JF Jr, Shanblatt ER, Nowak T, Dunning CAS, Fung GSK, et al. Technical performance of dual-contrast-agent K-edge imaging with four energy thresholds on a commercial photon counting detector CT. Med Phys. 2025; 52: e70063.
37. Feldkamp LA, Davis LC, Kress JW. Practical cone-beam algorithm. J Opt Soc Am A. 1984; 1: 612-9.
38. Persson M, Wang A, Pelc NJ. Detective quantum efficiency of photon-counting CdTe and Si detectors for computed tomography: a simulation study. J Med Imaging (Bellingham). 2020; 7: 043501.
39. Taguchi K, Iwanczyk JS. Vision 20/20: single photon counting x-ray detectors in medical imaging. Med Phys. 2013; 40: 100901.
40. Leng S, Bruesewitz M, Tao S, Rajendran K, Halaweish AF, Campeau NG, et al. Photon-counting detector CT: system design and clinical applications of an emerging technology. Radiographics. 2019; 39: 729-43.